Supplementary Information

A Rational Study on the Geometric and Electronic Properties of Single-atom Catalysts for Enhanced Catalytic Performance

Qi Xue[‡a], Yi Xie[‡b], Simson Wu[c], Tai-Sing Wu[d], Yun-Liang Soo[d], Sarah Day[e], Chiu C. Tang[e], Ho W. Man[a], Sha T. Yuen[b], Kwok-yin Wong[a], Ying Wang*[b], Benedict T.W. Lo*[a,f], Shik C.E. Tsang[c]

[a] State Key Laboratory of Chemical Biology and Drug Discovery, Department of Applied Biology and Chemical Technology
The Hong Kong Polytechnic University
Hong Kong, China
E-mail: benedict.tw.lo@polyu.edu.hk
[b] Department of Chemistry, The Chinese University of Hong Kong
Hong Kong, China
E-mail: ying.b.wang@cuhk.edu.hk
[c] Department of Chemistry
University of Oxford
Oxford, OX1 3QR, UK
[d] Department of Physics
National Tsing Hua University
Hsinchu, Taiwan
[e] Diamond Light Source Ltd
Harwell Science and Innovation campus
Didcot, Oxfordshire OX11 0DE, UK
[f] The Hong Kong Polytechnic University Shenzhen Research Institute
Shenzhen, China
‡ These authors contributed equally to this work as joint first authors.

1. Experimental Procedures

1.1 Material

UiO-66-NH_2

In a 100 mL hydrothermal vessel, 0.480 g zirconium tetrachloride and 0.372 g 2-aminoterephthalic acid (ATA) were dissolved in 40 mL N,N-dimethylformamide (DMF) solution, and heated isothermally at 120 °C for 12 hours. The UiO-66-NH_2 powder was subsequently collected by centrifugation, and washed by ethanol for 5 times. The powder was dried at 60 °C overnight.

The structural formula of the sample is calculated to be $Zr_6O_4(OH)_4(ATA)_{5.8}$, with low concentration linker defects by elemental analysis and thermogravimetric analysis (Figure S1). The Brunauer-Emmett-Teller surface area determined by N_2 adsorption is found to be 259 $m^2 g^{-1}$ (Figure S2).

UiO-66-NH_2 metalation

0.47 g obtained UiO-66-NH_2 were dispersed in 20 mL DMF through ultrasonication. 1 M bis(ethylenediamine)copper(II) hydroxide ('*bis*ENCu') solution was added dropwise to pristine UiO-66-NH_2 dispersed in N,N-dimethylformamide. Related Fe, Co, Ni and Zn precursors were used. The mixture was stirred at 25 °C for 12 hours to ensure homogeneity. Finally, the product was collected by centrifugation, washed twice by double distilled water and 3 times by ethanol, and dried at 60 °C overnight to obtain 1Cu-UiO-66-NH_2.The product was centrifuged and washed by double distilled water twice, and 3 times by ethanol. It was dried at 60 °C overnight. The samples were characterised by SEM (Figure S3) and TEM (Figure S4) before and after the modification of Cu single sites, which shows no obvious nanoparticles aggregation within the MOFs.

1.2 Methods

High-resolution synchrotron X-ray powder diffraction (SXRD) and Rietveld refinement

High-resolution SXRD data were collected at Beamline I11, Diamond Light Source, UK[1,2]. The energy of the incident X-ray flux was set at 15 keV. The tuned energy for each beamline emits the optimum X-ray flux to achieve high contrast (signal-to-noise ratio) and high angular resolution. The wavelength and the 2θ-zero point were calibrated using a diffraction pattern obtained from a high-quality silicon powder (NIST SRM640c). High-resolution SXRD data were obtained from the zeolite samples (loaded in 0.5-mm borosilicate capillaries) using the multi-analyser crystals (MAC) detectors. The patterns were collected in the 2θ range 0-150° with 0.001° data binning. Each diffraction pattern was collected for an hour for good statistics. In total, there are 490 *hkl* reflections measured (within the region of refinement (2θ = 2-60°), of which at least 100 independent *hkl* reflections are observed. From a mathematical perspective, the number of variables should not exceed the number of observables. In the Rietveld refinements performed in this work, the number of structural parameters has not exceeded 40.

Using the TOPAS 6.0 software, the lattice parameters were obtained using Pawley and Rietveld refinement analyses of the diffraction patterns were performed. The background curve was fitted by a Chebyshev polynomial with an average of 16 coefficients. The Thompson-Cox-Hastings (pseudo-Voigt) function was applied to describe the diffraction peaks[3]. The scale factor and lattice parameters were allowed to vary for all the histograms.

The final refined structural parameters for each data histogram were carried out using the Rietveld method with the fractional coordinates (*x*, *y*, *z*) and isotropic displacement factors (B_{eq}) for all atoms. In addition, the R_{wp} and *goodness-of-fit* values ($gof = R_{wp}/R_{exp}$) are helpful to indicate the quality of fit, where R_{exp} represents the quality of the data.

(i) Framework atoms

The crystallographic locations of the framework atoms may change slightly – a small deviation from the model by Wragg *et al*. Therefore, before the refinement of the entire structure with guest Cu site, the framework atoms and the positions of atoms were first refined. This was performed to avoid a miscalculation of the structure that reaches the global minimum of the refinement by changing the entire framework.

(ii) Fourier analysis

Over the 2θ range of 2-60°, the Fourier analysis was used to identify the positions with the highest remaining electron density in the framework, once the positions of the host atoms have been determined.

(iii) Inclusion of guest molecules

Based on the Fourier analysis, a Monte Carlo-based simulated annealing technique in which the guest Cu complex as rigid body was used to locate their positions in the UiO-66-NH_2. The guest Cu complex rigid body Z-matrices were refined, while keeping the fractional coordinates of the framework atoms fixed.

It was first applied to be simulated annealed using the Rietveld method (while the fractional coordinates of the framework were fixed). Thus, the simulated annealing technique ensures the correct number of Cu complexes.

After identifying the number and location of the Cu sites, the site occupancy factors (SOFs) were refined. Also, the bond and dihedral angles of Cu-OH in the rigid-body were refined with restraining to ± 20% from the optimised tetrahedral structures using Chem3D software. Then, the relevant parameters were relaxed to be refined by simulated annealing repeatedly for an hour to ensure the global minimum has been reached. The global minimum is indicated by the lowest R_{wp} and *gof* values. The Cu coordination geometry has been verified by the Rietveld refinement using a 5-coordinated square pyramidal rigid body Z-matrix with two bidentate ethylene diamine ligands and a hydroxyl group.

Several criteria were met to ensure the high quality and reliability of the refinement, namely, (i) the global minimum has been reached, (ii) the derived crystal structure fits chemical sense, (iii) reasonable systematic error values for all the refined parameters, and (iv) sensible SOF and B_{eq} values.

The B_{eq} were constrained in the following way: (i) all the framework Zr-sites share the same value as 0.6 $Å^2$, and the values for the framework O-sites as 2 $Å^2$, and (ii) the B_{eq} of the extra-framework atoms were all arbitrary fixed at 8-12 $Å^2$ (as B_{eq} is broadly accepted to be about proportional to measurement temperature as that of framework sites)[4–8]. The position errors of the Cu complex were estimated from the percentage errors of the translation and rotation axes of the rigid bodies.

High-throughput SXRD

High-throughput SXRD measurements for in situ desorption study were collected at beamline BL02B2 at SPring-8, Japan. The energy of the incident X-ray flux was set at 18 keV[2]. The wavelength (λ = 0.689556(2) Å) and the 2θ-zero point (ZP = -0.000015(2)°) were calibrated using a diffraction pattern obtained from a high-quality CeO_2 powder (NIST SRM674b). High-throughput SXRD data were obtained from the zeolite samples (loaded in 0.5-mm borosilicate capillaries)) using the MYTHEN detector. The patterns were collected in the 2θ range 2-78° with 0.006° data binning. Each SXRD pattern was collected for 5 min for each MYTHEN-2θ-step, *i.e.*, 10 min in total for MYTHEN data summation. This produced patterns with good signal-to-noise ratio (S/N). It should be particularly noted that the R-factors using the MYTHEN detectors (BL02B2) are generally higher than when MAC detectors (I11) are used due to the contrast (S/N) difference between the two instruments. Therefore, the quality of the Rietveld refinement should be best judged by the difference between the fitted and observed data.

For *in-situ* temperature programmed measurements, the samples were heated using an N_2-hot air blower at a ramping rate of 10 °C per min. Sequential SXRD measurements were collected at every 25 °C temperature step. The patterns were collected in the 2θ range 2-78° with 0.006° data binning. Each diffraction pattern was collected for 2 min.

In-situ powder XRD measurements

Pre-treated samples were finely sieved and loaded in 0.5-mm-borosilicate capillaries to reduce X-ray absorption problem. High-energy X-ray using Mo anode was used to optimise the spatial and angular resolution of the Bragg's reflections. Dynamic measurements were conducted at elevated temperatures at 5 °C min^{-1}. Each powder XRD pattern required 15 min of scanning time for a suitable and reliable signal-to-noise ratio.

Electrocatalytic CO_2 reduction reaction

5 mg of Cu-MOF was dispersed in a mixture of 0.99 mL of ethanol and 0.01 mL of Nafion and sonicated for 30 mins. It was then spray coated onto carbon paper to reach a loading of 0.6 mg/cm^2. Electrochemical measurements were conducted in a three-electrode system in a flow cell using on an electrochemical station (CH Instruments, 760E). The cathode and anode chambers were separated by an anion exchange membrane (Fumasep FAB-PK-130). Ni foam was used as the counter electrode. All potentials were measured with reference to a Ag/AgCl (saturated KCl) and converted to RHE scale according to E_RHE= E_(Ag/AgCl)+0.197+0.059×pH. Gaseous products were quantified with gas chromatography (GC2060, Ramiin, Shanghai) equipped with a flame ionisation detector (FID) and a thermal conductivity detector (TCD).

Cyclic voltammetry (CV) measurements

CV measurements were performed in a three-electrode arrangement containing the 200 μL sample (1 g/L) on ITO as working electrode, a platinum counter electrode, and Ag/AgCl (saturated KCl, aqueous) as reference. The electrodes were immersed in 0.1 M $LiClO_4$/DMF electrolyte solution and bubbled by N_2 for 5 minutes.

Results and Discussion

2.1 Figures

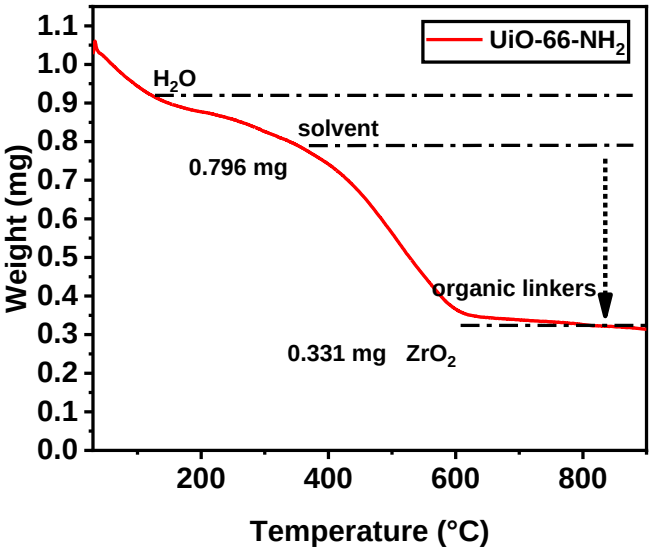

Figure S1. The TGA of the synthesised UiO-66-NH_2 to determine the quantity of linker defects.

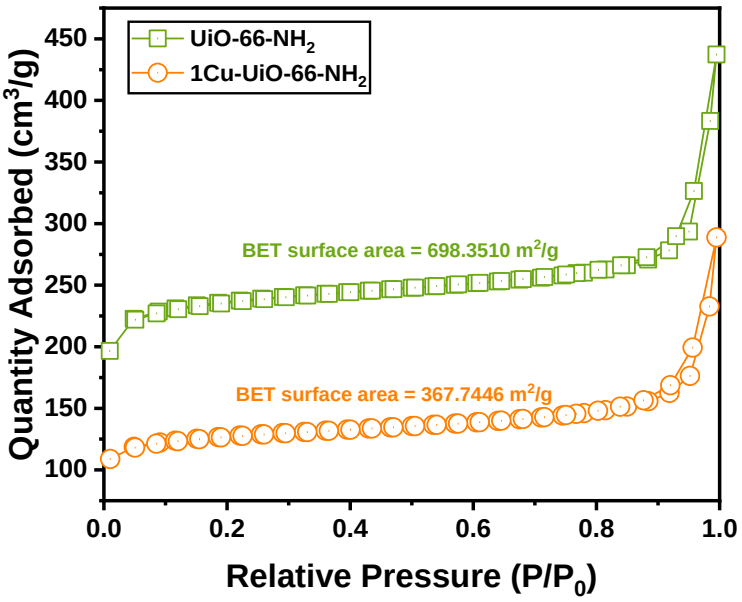

Figure S2. N_2 sorption isotherm of the UiO-66-NH_2 and Cu-UiO-66-NH_2. The surface area decreases by 47% from 698.4 m^2/g to 367.7 m^2/g, which can be attributed to the blockage of the void space of UiO-66-NH_2 by the metal species.

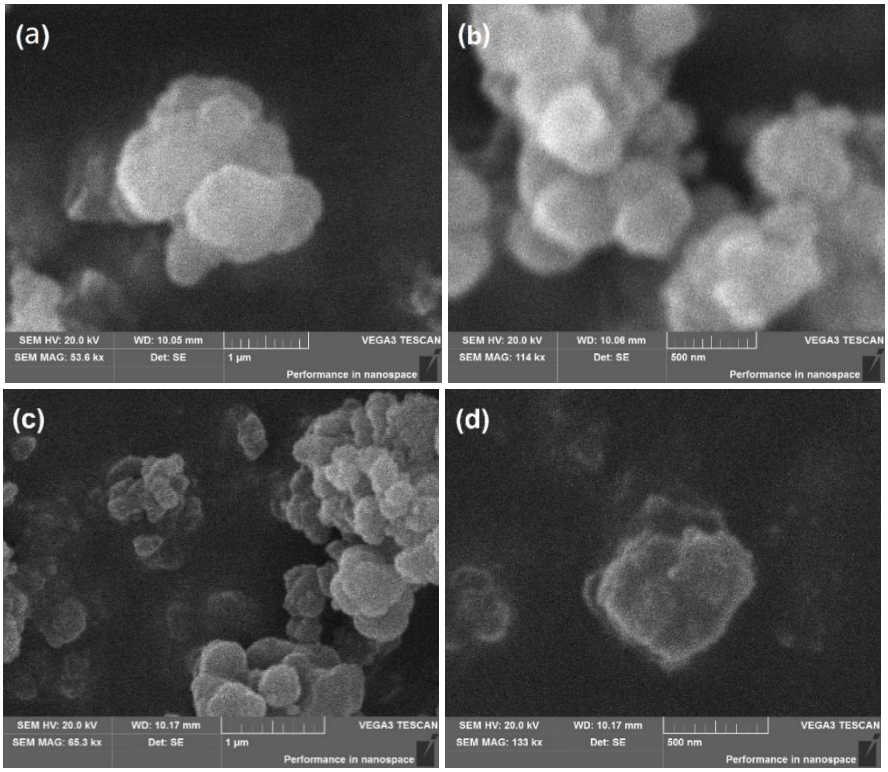

Figure S3. Scanning electron micrographs of (a) UiO-66-NH_2 and (b) the enlarged area. Micrographs of (c) 1Cu-UiO-66-NH_2 and (d) the enlarged area. No aggregated species can be observed after Cu metalation.

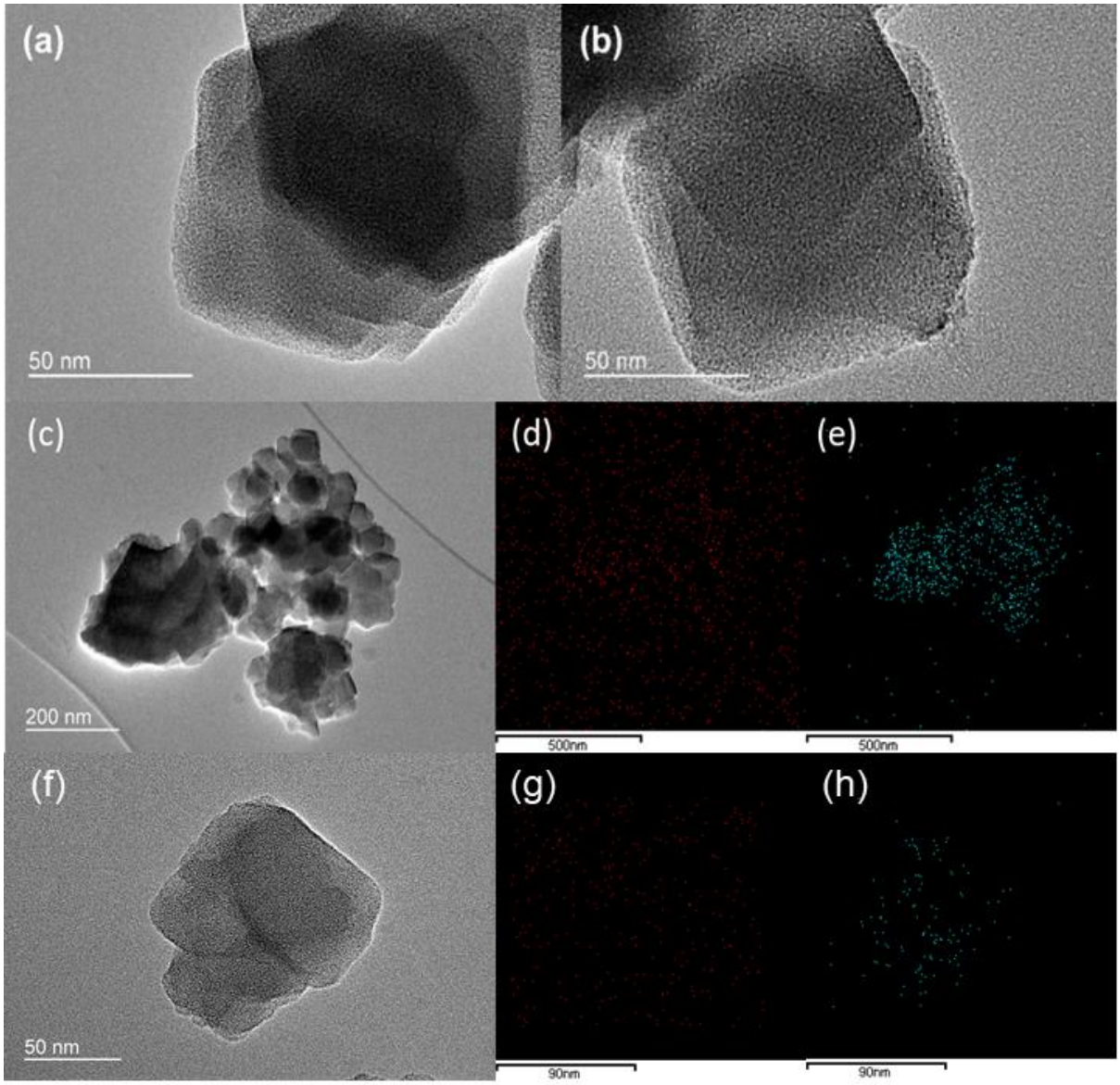

Figure S4. TEM images on Ni grid of the (a) pristine UiO-66-NH_2 and (b) 1Cu-UiO-66-NH_2. (c) Selected region for energy dispersive X-ray mapping analysis: (d) Cu and (e) Zr. (f) Enlarged region for energy dispersive X-ray mapping analysis: (g) Cu and (h) Zr. No aggregated species can be observed after Cu metalation.

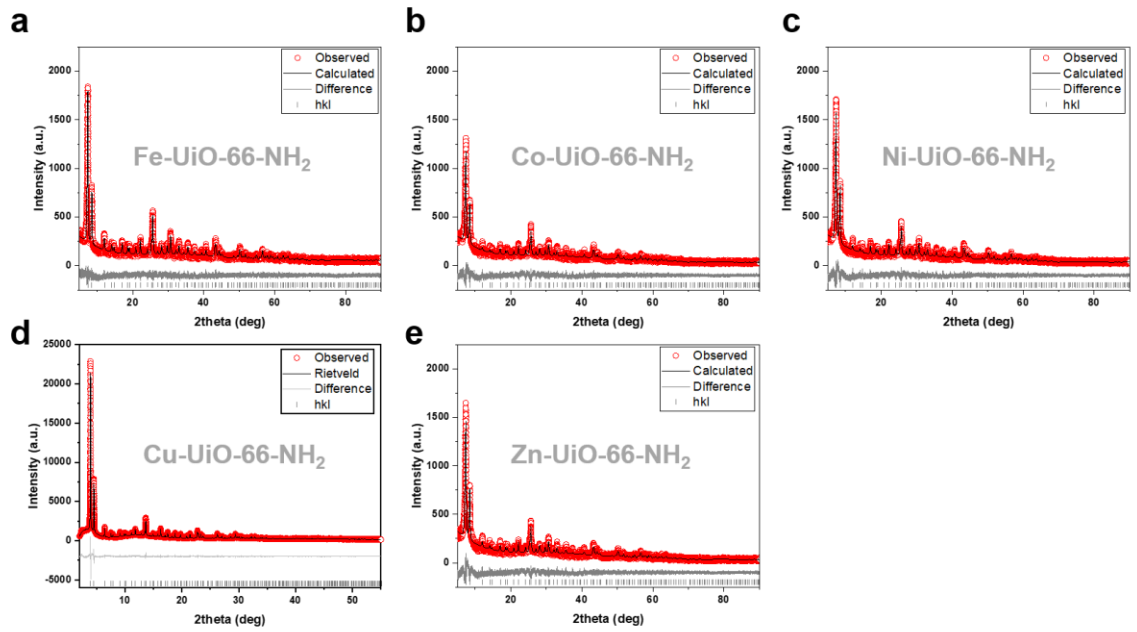

Figure S5. Powder XRD data and Rietveld refinement profiles of (**a**) 1Fe-UiO-66-NH_2, (**b**) 1Co-UiO-66-NH_2, (**c**) 1Ni-UiO-66-NH_2, (**d**) 1Cu-UiO-66-NH_2 and (**e**) 1Zn-UiO-66-NH_2. The structural and atomic parameters are summarised in Tables S2 and S4.

The diffraction peaks are generated from the interference of the atoms on a lattice plane. First, the incorporated metal sites contain relative high electron density, leading to higher X-ray absorption. This affects the overall scattering intensity, including the background and the peaks. Second, although the incorporation of different metal sites occurs periodically on the amino moieties, a subtle variation in the atomic parameters (mainly the site occupancy and fractional coordinates (x, y, z)) can greatly affect the peak intensity. As the metal sites are located at certain lattice planes, it directly changes the intensity (I(hkl)) of a given Bragg reflection, where *I(hkl) is proportional to the square of the structure factor of the corresponding lattice plane (F(hkl))*. Meanwhile, the structure factor is calculated as a function of the atomic coordinates of different species.

$$F_{hkl} = \Sigma f_j g_j [exp-2\pi i(hx_j+ky_j+lz_j)] exp(-B_j sin2\theta/\lambda^2)$$

where

the sum is over all atoms in the unit cell,

f_j is the scattering factor of the atom j,

g_j is the site occupancy factor (SOF),

x_j, y_j, and z_j are the fractional atomic coordinates, and

B_j is a measure of the root-mean-square amplitude of atomic vibration.

As the crystallinity of the MOFs is not altered upon metalation, we can apply the Rietveld refinement (whole pattern refinement technique) to elucidate the atomic parameters of the structure.

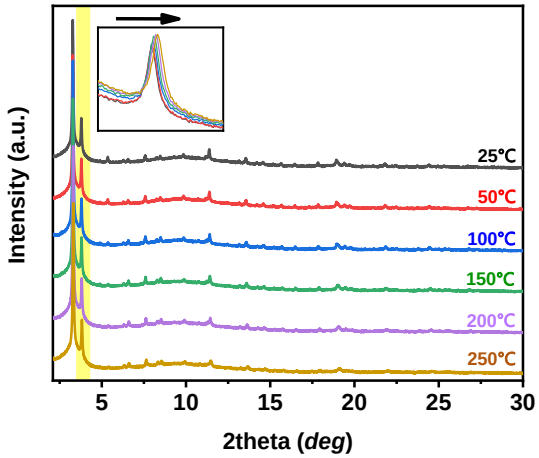

Figure S6. In-situ temperature-programmed SXRD of 1Cu-UiO-66-NH_2 (λ = 0.689556(2) Å; data collected at Spring-8 BL02B2). Inset: selected zoom-in of (002) reflection.

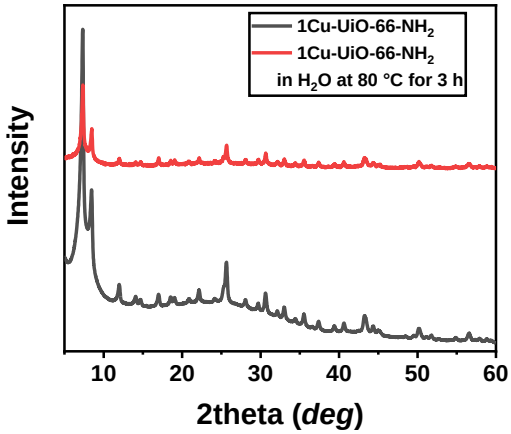

Figure S7. The powder XRD patterns of 1Cu-UiO-66-NH_2 suspended in H_2O before and after heated to 80 °C for 3 h.

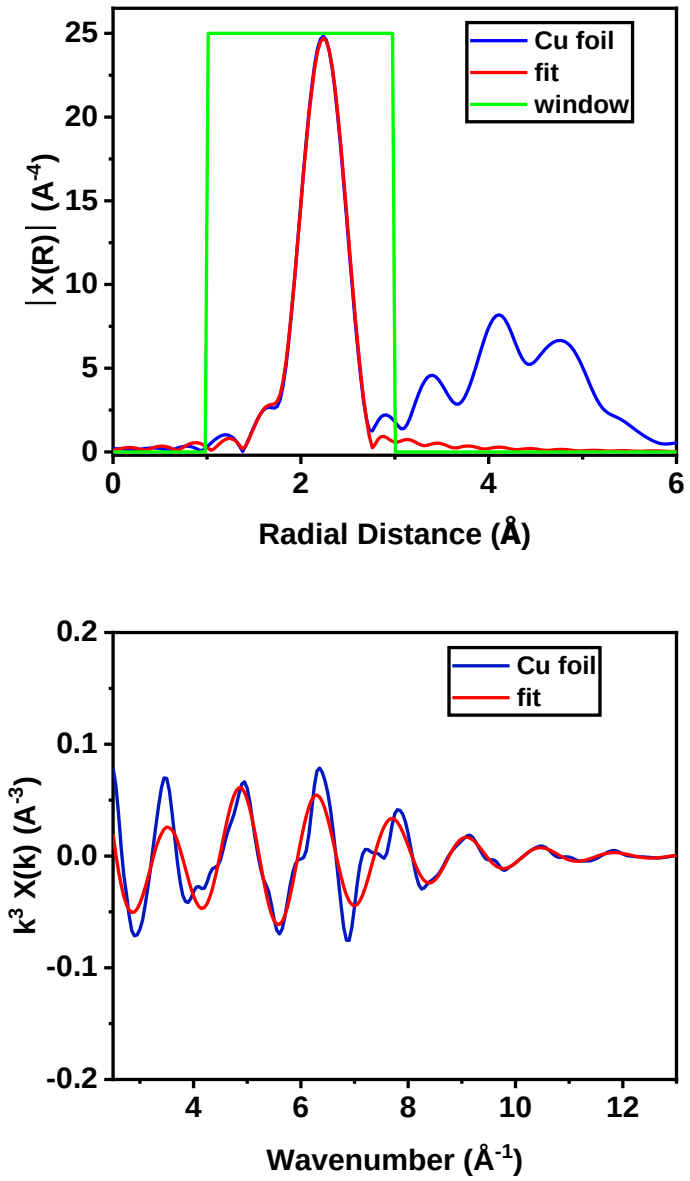

Figure S8(a). Fourier-transformed Cu K-edge of extended X-ray absorption fine spectroscopy (EXAFS) spectrum of Cu foil and k^3 weighted χ function of the EXAFS spectra of Cu foil.

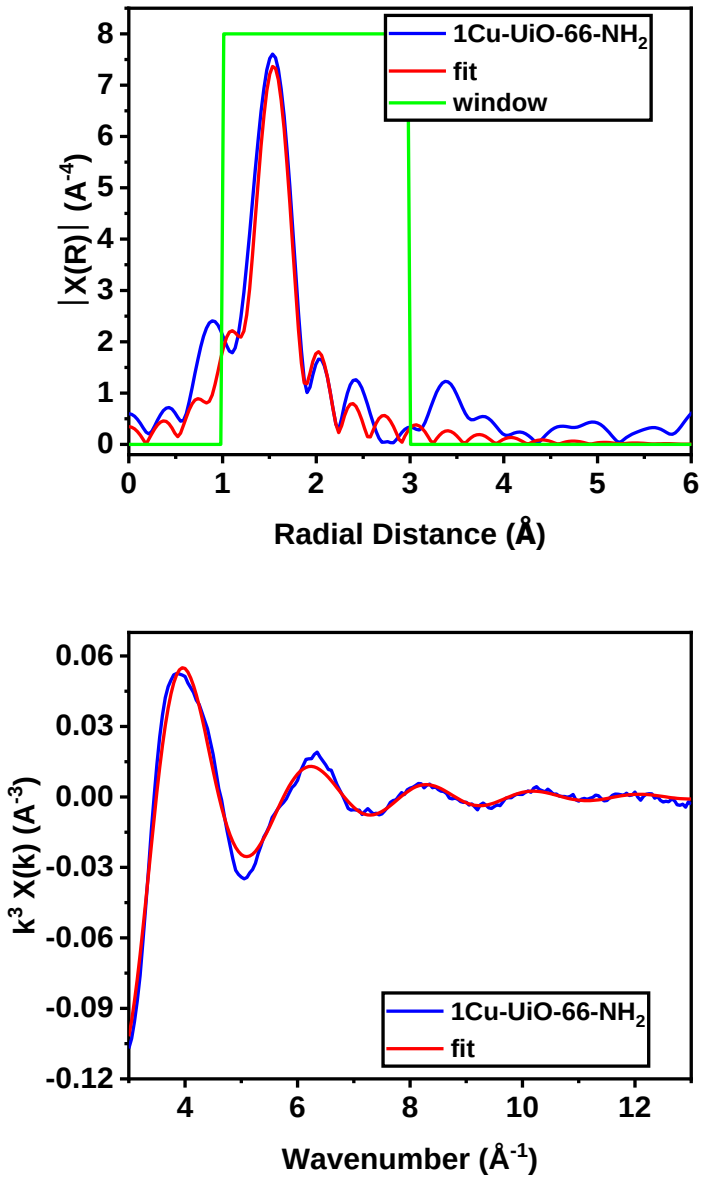

Figure S8(b). Fourier-transformed Cu K-edge of EXAFS spectrum and k^3 weighted χ function of the EXAFS spectrum of 1Cu-UiO-66-NH_2.

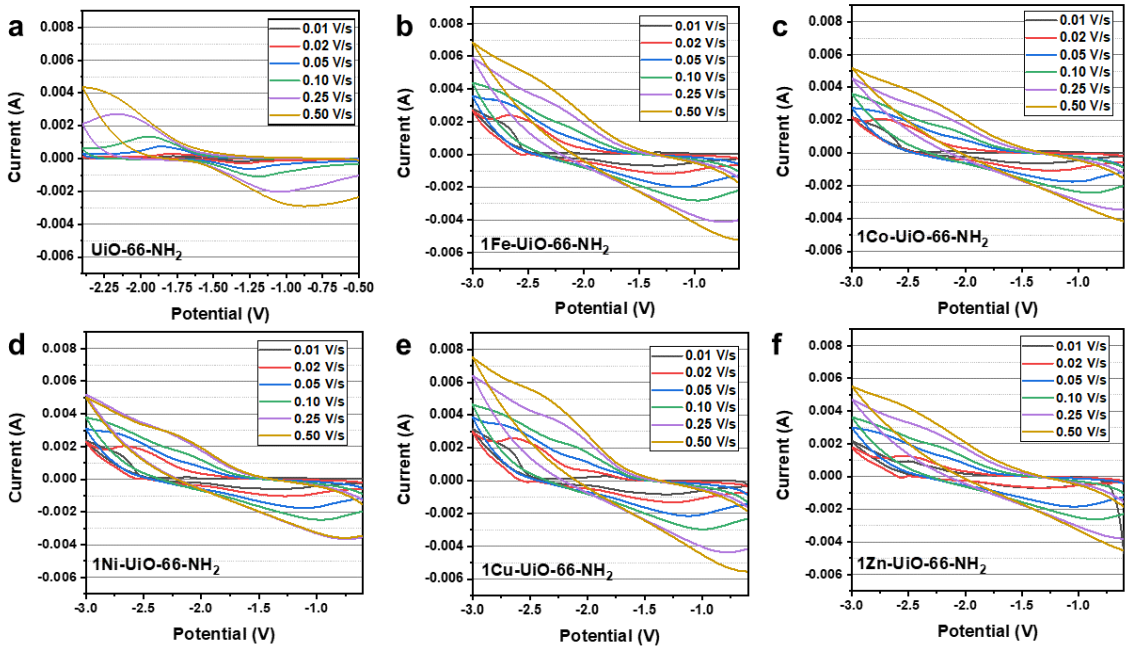

Figure S9. Cyclic voltammetry of UiO-66-NH_2, 1Fe-, 1Co-, 1Ni-, 1Cu-, and 1Zn-UiO-66-NH_2.

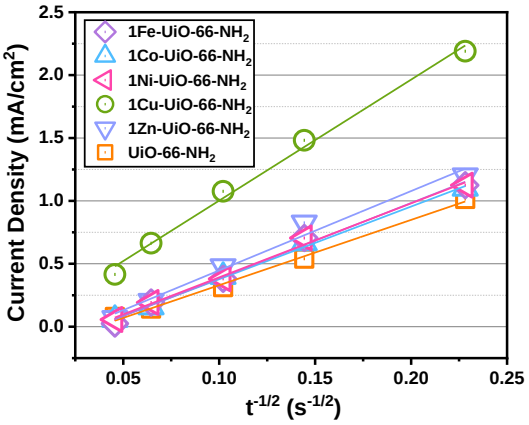

Figure S10. The Cottrell plots (I(t) *vs* $t^{-1/2}$) of UiO-66-NH_2 when compared with those incorporated with different metal species.

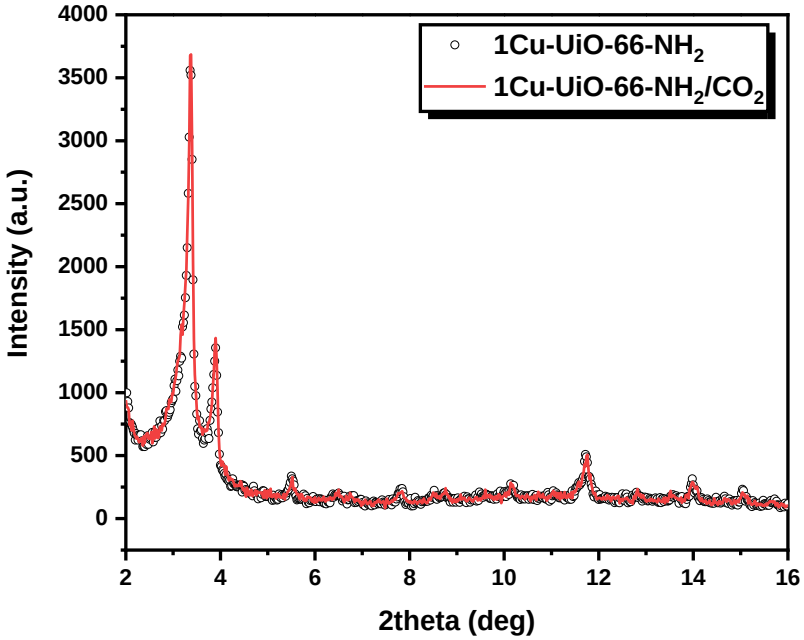

Figure S11. The powder XRD patterns of 1Cu-UiO-66-NH_2 and 1Cu-UiO-66-NH_2 pre-adsorbed with CO_2.

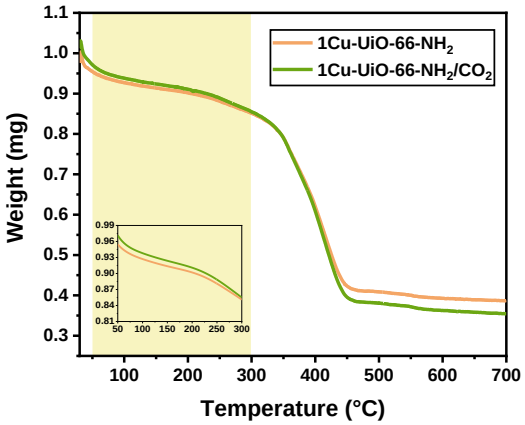

Figure S12. TGA of 1Cu-UiO-66-NH_2 and 1Cu-UiO-66-NH_2 pre-adsorbed with CO_2.

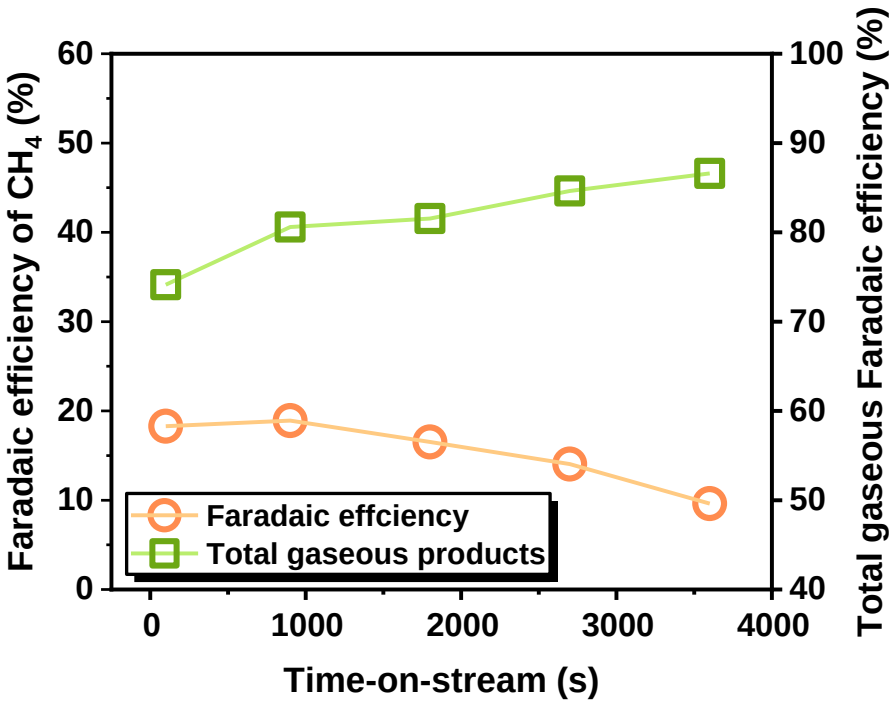

Figure S13. The Faradaic efficiency of CH_4 and total gaseous products of eCO_2RR by 1Cu-UiO-66-NH_2 remained stable within 3600 s.

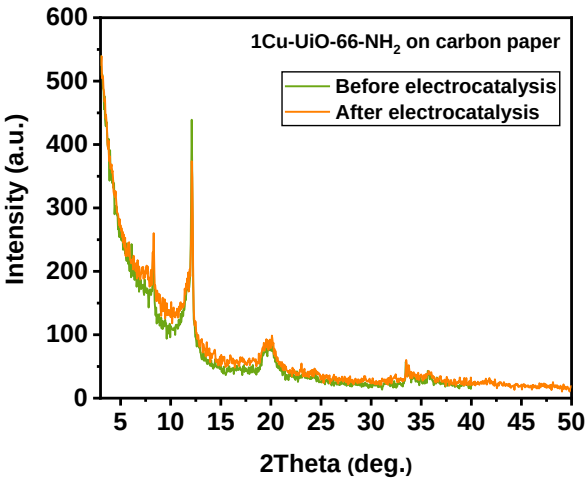

Figure S14. 1Cu-UiO-66-NH_2 on carbon paper before (green) and after (orange) eCO_2RR.

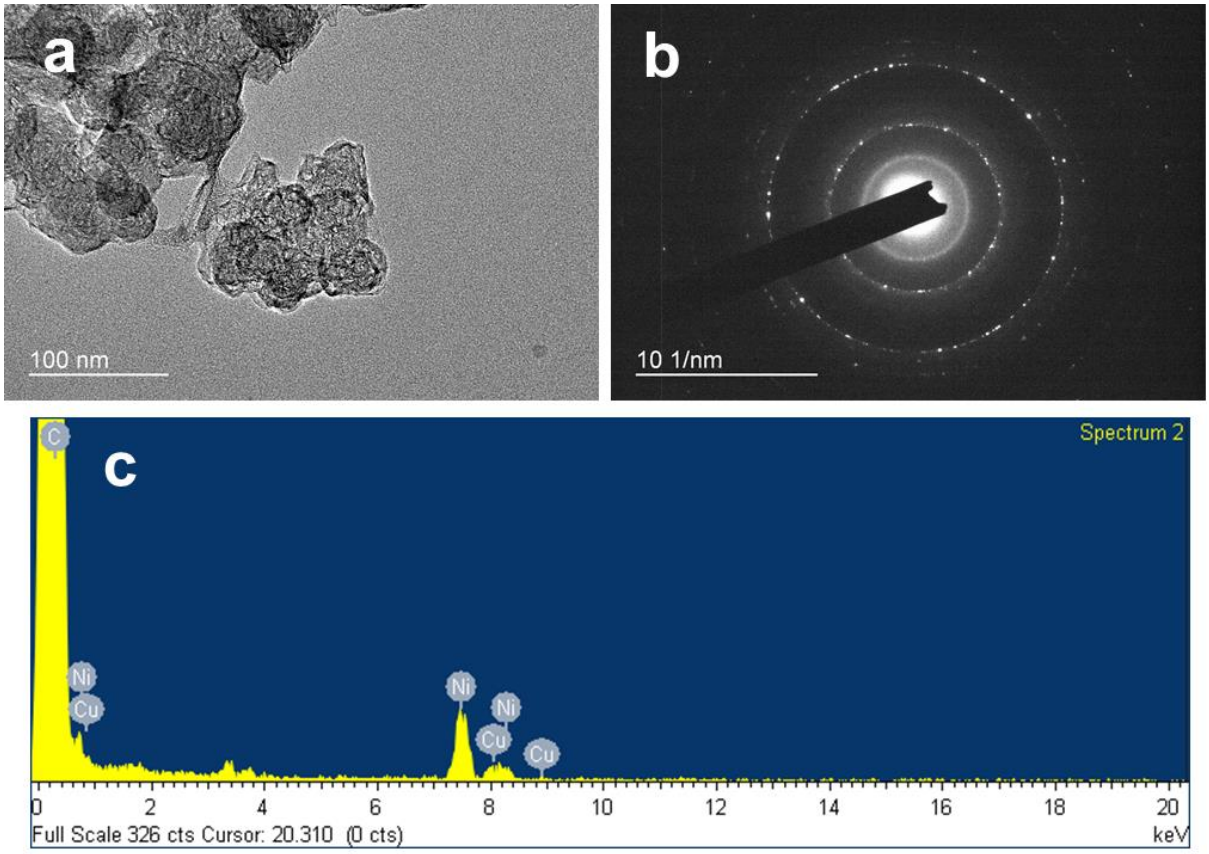

Figure S15. TEM image of (a) 1Cu-UiO-66-NH_2 post eCO_2RR (on Ni grid). The morphology of MOF is remained. No apparent aggregation is seen. (b) The corresponding electron diffraction pattern. (c) The energy-dispersive X-ray spectroscopic analysis.

2.2 Tables

Table S1(a). Elemental analysis by Rietveld refinement. The number of SACs per unit cell of UiO-66-NH_2 is calculated by multiplying the site occupancy factors (from Rietveld refinement) by ×48 (*Fm-3m*).

Sample	Metal (site occupancy factor)	# SACs per unit cell	Zr (site occupancy factor)
1Fe-UiO-66-NH_2	0.233	11.2	1
1Co-UiO-66-NH_2	0.168	8.1	1
1Ni-UiO-66-NH_2	0.135	6.5	1
1Cu-UiO-66-NH_2	0.091	4.4	1
1Zn-UiO-66-NH_2	0.086	4.1	1

Table S1(b). Elemental analysis by inductively coupled plasma optical emission spectroscopy of 1Cu-UiO-66-NH_2 before and after heating in water at 80 °C for 3 h.

1Cu-UiO-66-NH_2	Cu (mol L^{-1})	Zr (mol L^{-1}, normalised)
Before heating	0.0012	0.0827
Heating in water at 80 °C for 3 h	0.0016	0.0827

Table S2. Crystallographic parameters from the powder XRD measurements of 1Cu-UiO-66-NH_2 after immersing in solution for 3 hours.

	Pristine	**After**
Diffractometer	Rigaku SmartLab	Rigaku SmartLab
Energy	9 kW	9 kW
X-ray tube	Cu	Cu
Wavelength (Å)	1.5406	1.5406
2θ - zero point (°)	-0.0518(20)	-0.0446(63)
Space group	*Fm-3m*	*Fm-3m*
Crystal system	Cubic	Cubic
a (Å)	20.7992(23)	20.7781(79)
V (Å^3)	8998(3)	8970(10)
LVol-IB (nm)	133(12)	26(7)
2θ range for refinement (°)	5-60	5-60
Detector	2-D HyPix-3000	2-D HyPix-3000
Number of parameters	29	29
Number of *hkl*s	96	96
Refinement methods	Pawley	Pawley
$R_{wp}/R_{exp}/R_p$ (%)	5.845/4.434/4.706	6.084/5.700/4.844
gof	1.318	1.067

LVol-IB: volume-weighted mean crystallite sizes calculated using the uses full-width-half-maximum and Integral breadth; R_{wp}: weighted profile; R_{exp}: expected; R_p: profile; *gof*: goodness-of-fit.

Table S3(a). Atomic parameters derived from the Rietveld refinement of the PXRD measurement of 1Fe-UiO-66-NH_2, measured at 25 °C (R_{wp} = 11.841%).

Species	Atom	*x*	*y*	*z*	SOF	B_{eq} (Å^2)	Wyckoff letter
MOF-host	Zr1	0.1325(2)	0	0	1	1	*d*
	O2	0.0584(5)	0.0584(5)	0.0584(5)	1	2	*f*
	C1	0.1523	0	0.1523	1	2	*h*
	C2	0.20363	0	0.20363	1	2	*h*
	C3	0.26724	0	0.18658	1	2	*j*
	O1	0.16828	0	0.09268	1	2	*j*
	N1	0.28404	0	0.1239	0.25	2	*j*
Extra-framework site	Fe1	0.2912(3)	0.0892(14)	0.1004(14)	0.233(2)	6	*l*

SOF: site occupancy factor; B_{eq}: isotropic displacement factor.

Table S3(b). Atomic parameters derived from the Rietveld refinement of the PXRD measurement of 1Co-UiO-66-NH_2, measured at 25 °C (R_{wp} = 11.275%).

Species	Atom	*x*	*y*	*z*	SOF	B_{eq} (Å^2)	Wyckoff letter
MOF-host	Zr1	0.1325(2)	0	0	1	1	*d*
	O2	0.0531(5)	0.0531(5)	0.0531(5)	1	2	*f*
	C1	0.1523	0	0.1523	1	2	*h*
	C2	0.20362	0	0.20362	1	2	*h*
	C3	0.26721	0	0.18657	1	2	*j*
	O1	0.16827	0	0.09269	1	2	*j*
	N1	0.28401	0	0.1239	0.25	2	*j*
Extra-framework site	Co1	0.3105(6)	-0.091(4)	0.096(4)	0.168(2)	6	*l*

SOF: site occupancy factor; B_{eq}: isotropic displacement factor.

Table S3(c). Atomic parameters derived from the Rietveld refinement of the PXRD measurement of 1Ni-UiO-66-NH_2, measured at 25 °C (R_{wp} = 10.962%).

Species	Atom	*x*	*y*	*z*	SOF	B_{eq} (Å^2)	Wyckoff letter
MOF-host	Zr1	0.1320(2)	0	0	1	1	*d*
	O2	0.0521(4)	0.0521(4)	0.0521(4)	1	2	*f*
	C1	0.1523	0	0.1523	1	2	*h*
	C2	0.20362	0	0.20362	1	2	*h*
	C3	0.26722	0	0.18658	1	2	*j*
	O1	0.16827	0	0.09269	1	2	*j*
	N1	0.28402	0	0.1239	0.25	2	*j*
Extra-framework site	Ni1	0.3146(6)	-0.086(3)	0.094(3)	0.135(2)	6	*l*

SOF: site occupancy factor; B_{eq}: isotropic displacement factor.

Table S3(d). Atomic parameters derived from the Rietveld refinement of the SXRD measurement of 1Cu-UiO-66-NH_2, measured at 25 °C (R_{wp} = 9.510%).

Species	Atom	*x*	*y*	*z*	SOF	B_{eq} (Å^2)	Wyckoff letter
MOF-host	Zr1	0.12050(8)	0	0	1	0.6	*d*
	O2	0.0583(2)	0.0583(2)	0.0583(2)	1	2	*f*
	C1	0.15211(10)	0	0.15211(10)	1	2	*h*
	C2	0.20343(10)	0	0.20343(10)	1	2	*h*
	C3	0.26704(10)	0	0.18639(10)	1	2	*j*
	O1	0.16808(10)	0	0.09250(10)	1	2	*j*
	N1	0.28383(10)	0	0.12371(10)	0.25	2	*j*
Cu	Cu1	0.3323(8)	0.1116(10)	0.0827(12)	0.091(1)	8	*l*
	N2	0.244(3)	0.117(10)	0.115(9)	0.091(1)	10	*l*
	N3	0.308(4)	0.040(4)	0.028(6)	0.091(1)	10	*l*
	C6	0.202(3)	0.075(12)	0.076(13)	0.091(1)	12	*l*
	C7	0.243(6)	0.017(8)	0.045(11)	0.091(1)	12	*l*
	O10	0.320(7)	0.177(9)	0.149(10)	0.091(1)	10	*l*

SOF: site occupancy factor; B_{eq}: isotropic displacement factor.

Table S3(e). Atomic parameters derived from the Rietveld refinement of the PXRD measurement of 1Zn-UiO-66-NH_2, measured at 25 °C (R_{wp} = 11.352%).

Species	Atom	*x*	*y*	*z*	SOF	B_{eq} (Å^2)	Wyckoff letter
MOF-host	Zr1	0.1337(3)	0	0	1	1	*d*
	O2	0.0525(4)	0.0525(4)	0.0525(4)	1	2	*f*
	C1	0.1551(3)	0	0.1551(3)	1	2	*h*
	C2	0.2064(3)	0	0.2064(3)	1	2	*h*
	C3	0.2700(3)	0	0.1894(3)	1	2	*j*
	O1	0.1711(3)	0	0.0956(3)	1	2	*j*
	N1	0.2868(3)	0	0.1268(3)	0.25	2	*j*
Extra-framework site	Zn1	0.3197(9)	-0.069(6)	0.075(6)	0.086(2)	6	*l*

SOF: site occupancy factor; B_{eq}: isotropic displacement factor.

Table S4(a). EXAFS fitting result of Cu foil.

Scattering Path	Bond Length (Å)	Coordination number (CN)	Debye-Waller factor ($Å^2$)
Cu-Cu	2.54(1)	12	0.009(1)

Amplitude reduction factor: 0.89
k-range: 3-12.5 $Å^{-1}$
R-range: 1-3 Å
Energy difference between theoretical path and calculated path: -7.7 eV
R-factor: 0.9%

Table S4(b). EXAFS fitting result of 1Cu-UiO-66-NH_2.

Scattering Path	Bond Length (Å)	CN	Debye-Waller factor ($Å^2$)
Cu-N	1.97(2)	4.2(2)	0.004(1)

k-range: 3-12.3 $Å^{-1}$
R-range: 1-3 Å
Energy difference between theoretical path and calculated path: -3.3 eV
R-factor: 1.0%

Table S5. The dynamic change in the lattice parameters and R-factors of the in-situ XRD measurements of 1Cu-UiO-66-NH_2.The estimated standard deviation values (systematic errors) of the lattice parameters were calculated by TOPAS 6.0, in the range of ± 0.0050-0.0060 Å.

Temperature (°C)	**Lattice parameter *a* (Å)**	**R_{wp} (%)**	**R_{exp} (%)**	**χ^2**
25	20.7920	8.4584	5.823	1.4526
30	20.7925	8.3507	5.8262	1.4333
40	20.7955	8.4644	5.8461	1.4479
50	20.8105	8.1794	5.8576	1.3964
60	20.8152	8.3802	5.8506	1.4324
70	20.8183	8.5604	5.8555	1.4619
80	20.8056	8.0313	5.8576	1.3711
90	20.8106	8.1924	5.8449	1.4016
100	20.8035	8.6215	5.8224	1.4807
110	20.7703	7.8304	5.8109	1.3475
120	20.7574	7.8769	5.7843	1.3618
130	20.7569	8.5293	5.7554	1.482
140	20.7580	7.8339	5.6776	1.3798
150	20.7522	8.0694	5.6336	1.4324
160	20.7468	8.2306	5.614	1.4661
170	20.7426	8.0402	5.6044	1.4346
180	20.7485	8.452	5.6136	1.5056
190	20.7414	8.1729	5.6065	1.4578
200	20.7443	7.7616	5.614	1.3825
210	20.7419	8.298	5.6153	1.4778
220	20.7491	8.1404	5.6325	1.4452
230	20.7435	8.1934	5.6156	1.4591
240	20.7396	8.1935	5.6307	1.4552
250	20.7360	7.9738	5.6392	1.414
260	20.7304	7.9701	5.6613	1.4078
270	20.6892	8.0137	5.7234	1.4001
280	20.5895	8.4695	5.8377	1.4508

Table S6. The dynamic change in the lattice parameters and R-factors of the in-situ XRD measurements of 1Cu-UiO-66-NH_2 with adsorbed CO_2. The estimated standard deviation values (systematic errors) of the lattice parameters were calculated by TOPAS 6.0, in the range of ± 0.0050-0.0060 Å.

Temperature (°C)	**Lattice parameter *a* (Å)**	**R_{wp} (%)**	**R_{exp} (%)**	**χ^2**
25	20.7838	8.0931	5.7475	1.4081
30	20.7845	8.3032	5.7347	1.4479
40	20.7968	7.8966	5.7703	1.3685
50	20.7947	8.2946	5.7798	1.4351
60	20.7992	8.1327	5.7770	1.4078
70	20.8039	8.2461	5.8044	1.4207
80	20.7923	8.5363	5.7776	1.4775
90	20.7918	8.0478	5.7797	1.3924
100	20.7819	8.0181	5.7544	1.3934
110	20.7643	8.2681	5.7426	1.4398
120	20.7749	8.2233	5.7088	1.4405
130	20.7594	7.8508	5.6564	1.3879
140	20.7568	7.6251	5.5529	1.3732
150	20.7476	7.8307	5.5411	1.4132
160	20.7500	7.8832	5.5227	1.4274
170	20.7482	7.9409	5.5253	1.4372
180	20.7396	7.8685	5.5321	1.4223
190	20.7447	7.9486	5.5243	1.4388
200	20.7416	7.9336	5.5160	1.4383
210	20.7316	8.3084	5.5398	1.4998
220	20.7410	8.1320	5.5392	1.4681
230	20.7419	7.7465	5.5348	1.3996
240	20.7339	7.7868	5.5477	1.4036
250	20.7139	7.6755	5.5849	1.3743
260	20.6819	7.5855	5.5830	1.3587
270	20.6819	7.9530	5.6304	1.4125
280	20.5531	8.0570	5.7819	1.3935

Table S7. The electrochemical catalytic activities evaluated at different current densities.

Sample	j (mA cm^{-2})	CO FE (%)	CH_4 FE (%)	C_2H_4 FE (%)	H_2 FE (%)	Total FE of gaseous products (%)	Time-on-stream (s)
1Cu-UiO-66-NH_2	-75	4.20	14.54	13.52	27.85	60.12	100
1Cu-UiO-66-NH_2	-75	3.43	16.32	5.00	47.75	72.51	900
1Cu-UiO-66-NH_2	-75	3.25	9.66	0.01	64.85	77.78	1800
1Cu-UiO-66-NH_2	-100	4.07	16.08	14.6	29.45	64.21	100
1Cu-UiO-66-NH_2	-100	4.47	17.45	8.64	40.33	70.91	900
1Cu-UiO-66-NH_2	-100	5.49	16.40	3.95	50.09	75.95	1800
1Cu-UiO-66-NH_2	-200	2.39	12.49	11.12	34.62	60.64	100
1Cu-UiO-66-NH_2	-200	2.59	10.28	3.52	55.98	72.40	900
1Cu-UiO-66-NH_2	-200	3.14	10.27	0.98	60.23	74.64	1800
1Fe-UiO-66-NH_2	-100	0.74	0.00	0.00	99.83	100.56	100
1Co-UiO-66-NH_2	-100	12.79	2.60	0.00	53.40	68.78	100
1Co-UiO-66-NH_2	-100	8.27	1.05	0.00	77.57	86.89	900
1Ni-UiO-66-NH_2	-100	7.27	0.00	0.00	83.96	91.23	100
1Ni-UiO-66-NH_2	-100	7.66	0.00	0.00	89.43	97.09	900
1Zn-UiO-66-NH_2	-100	10.89	2.14	0.00	67.43	80.45	100
1Zn-UiO-66-NH_2	-100	5.99	0.00	0.00	89.59	95.57	900
UiO-66-NH_2	-50	9.82	0.00	0.00	48.53	58.35	100
UiO-66-NH_2	-50	11.57	0.00	0.00	67.91	79.48	900
UiO-66-NH_2	-100	0.68	0.00	0.00	68.62	69.30	100
UiO-66-NH_2	-100	1.88	0.00	0.00	73.10	74.98	900
UiO-66-NH_2	-100	1.83	0.00	0.00	72.85	74.68	1800
Carbon paper	-50	4.01	0.00	0.00	75.14	79.15	100

Table S8. The Faradaic efficiency (FE, %) of liquid products of 1Cu-UiO-66-NH_2.

Time-on-stream (s)	EtOH	AcO^-	$HCOO^-$	Total FE of liquid products (%)
100	0	17.05	0	17.05
900	5.60	2.97	11.14	19.73
1800	5.01	3.40	10.97	19.38
2700	0	0	3.35	3.35
3600	3.01	0.38	0.19	3.58

3. References

[1] S.P.Thompson, J.E.Parker, J.Marchal, J.Potter, A.Birt, F.Yuan, R.D.Fearn, A.R.Lennie, S.R.Street, C.C.Tang, Fast X-ray powder diffraction on I11 at Diamond, J. Synchrotron Radiat. 18 (2011) 637–648. https://doi.org/10.1107/S0909049511013641.

[2] S.P.Thompson, J.E.Parker, J.Potter, T.P.Hill, A.Birt, T.M.Cobb, F.Yuan, C.C.Tang, Beamline I11 at Diamond: A new instrument for high resolution powder diffraction, Rev. Sci. Instrum. 80 (2009). https://doi.org/10.1063/1.3167217.

[3] P.Thompson, D.E.Cox, J.B.Hastings, Rietveld Refinement of Debye-Scherrer Synchrotron X-ray Data from Al2O3, J. Appl. Crystallogr. 20 (1987) 79–83. https://doi.org/10.1107/S0021889887087090.

[4] D.Watkin, Uequiv: its past, present and future, Acta Crystallogr. Sect. B Struct. Sci. 56 (2000) 747–749.

[5] R.I.Cooper, A.L.Thompson, D.J.Watkin, CRYSTALS enhancements: Dealing with hydrogen atoms in refinement, J. Appl. Crystallogr. 43 (2010) 1100–1107. https://doi.org/10.1107/S0021889810025598.

[6] H.VanKoningsveld, High-temperature (350 K) orthorhombic framework structure of zeolite H-ZSM-5, Acta Crystallogr. Sect. B Struct. Sci. 46 (1990) 731–735.

[7] B.F.Mentzen, Characterization of guest molecules adsorbed on zeolites of known structure by combined x-ray powder profile refinements and conventional difference-fourier techniques. Part II-Localization of the n-hexane, TPA and p-xylene guests in a pentasil type zeoli, Mater. Res. Bull. 22 (1987) 489–496.

[8] R.Goyal, A.N.Fitch, H.Jobic, Powder neutron and X-ray diffraction studies of benzene adsorbed in zeolite ZSM-5, J. Phys. Chem. B. 104 (2000) 2878–2884.

[9] H.Zhang, J.Li, Q.Tan, L.Lu, Z.Wang, G.Wu, Metal–organic frameworks and their derived materials as electrocatalysts and photocatalysts for CO2 reduction: progress, challenges, and perspectives, Chem. Eur. J. 24 (2018) 18137–18157.

[10] X.Jiang, H.Wu, S.Chang, R.Si, S.Miao, W.Huang, Y.Li, G.Wang, X.Bao, Boosting CO2 electroreduction over layered zeolitic imidazolate frameworks decorated with Ag2O nanoparticles, J. Mater. Chem. A. 5 (2017) 19371–19377. https://doi.org/10.1039/c7ta06114e.

[11] C.-W.Kung, C.O.Audu, A.W.Peters, H.Noh, O.K.Farha, J.T.Hupp, Copper Nanoparticles Installed in Metal− Organic Framework Thin Films are Electrocatalytically Competent for CO 2 Reduction, (2017). https://doi.org/10.1021/acsenergylett.7b00621.

[12] K.Zhao, Y.Liu, X.Quan, S.Chen, H.Yu, CO 2 Electroreduction at Low Overpotential on Oxide-Derived Cu/ Carbons Fabricated from Metal Organic Framework, (2017). https://doi.org/10.1021/acsami.6b15402.

[13] Y.Guo, H.Yang, X.Zhou, K.Liu, C.Zhang, Z.Zhou, C.Wang, W.Lin, Electrocatalytic reduction of CO 2 to CO with 100% faradaic efficiency by using pyrolyzed zeolitic imidazolate frameworks supported on carbon nanotube networks †, (2017). https://doi.org/10.1039/c7ta08431e.

[14] C.Zhao, X.Dai, T.Yao, W.Chen, X.Wang, J.Wang, J.Yang, S.Wei, Y.Wu, Y.Li, Ionic Exchange of Metal−Organic Frameworks to Access Single Nickel Sites for Efficient Electroreduction of CO 2, J. Am. Chem. Soc. 139 (2017). https://doi.org/10.1021/jacs.7b02736.

[15] X.Wang, Z.Chen, X.Zhao, T.Yao, W.Chen, R.You, C.Zhao, G.Wu, J.Wang, W.Huang, J.Yang, X.Hong, S.Wei, Y.Wu, Y.Li, Regulation of Coordination Number over Single Co Sites: Triggering the Efficient Electroreduction of CO2, Angew. Chemie - Int. Ed. 57 (2018) 1944–1948. https://doi.org/10.1002/anie.201712451.

[16] X.Wang, Z.Chen, X.Zhao, T.Yao, W.Chen, R.You, C.Zhao, G.Wu, J.Wang, W.Huang, J.Yang, X.Hong, S.Wei, Y.Wu, Y.Li, Regulation of Coordination Number over Single Co Sites: Triggering the Efficient Electroreduction of CO ₂, Angew. Chemie. 130 (2018) 1962–1966. https://doi.org/10.1002/ange.201712451.

[17] Y.Ye, F.Cai, H.Li, H.Wu, G.Wang, Y.Li, S.Miao, S.Xie, R.Si, J.Wang, X.Bao, Surface functionalization of ZIF-8 with ammonium ferric citrate toward high exposure of Fe-N active sites for efficient oxygen and carbon dioxide electroreduction, Nano Energy. 38 (2017) 281–289. https://doi.org/10.1016/j.nanoen.2017.05.042.

[18] F.Pan, H.Zhang, K.Liu, D.Cullen, K.More, M.Wang, Z.Feng, G.Wang, ⊥ Gang Wu, Y.Li, Unveiling Active Sites of CO2 Reduction on Nitrogen-Coordinated and Atomically Dispersed Iron and Cobalt Catalysts, 8 (2018). https://doi.org/10.1021/acscatal.8b00398.